Constitutive Models for Root-Soil Contact Interface Considering Hydro-Mechanical Effects

Haruka Tomobe

2020

1 Introduction

Plant-soil mechanical interaction plays an essential role in sustaining water supply and plant production, and the interaction is a significant research subject from the standpoints of geotechnical engineering and plant production science for decades. It is widely accepted that soils are vital materials for building and supporting artificial/biological agricultural objects such as dams, irrigation/drainage open channels, agricultural fields, as well as crops. As can be seen on earth dams and embankments, soil domains are covered by vegetation which interacts with the microscopic structure and stability of soils (Ali and Osman, 2008; Liang et al., 2017). Since soil behavior is affected by microscopic soil structure such as void ratio, contact conditions of soil particles, and contamination of natural/artificial fibers, the presence of the plant roots affects the mechanical characteristics of soil structure. During the last four decades, it has been reported that plant roots often increase the shear strength of soils by reinforcing apparent cohesion and that the reinforcement is beneficial to increase the stability of soils (Endo 1980; Gray and Ohashi., 1983; Abe and Ziemer, 1991;Docker and Hubble., 2008; Hejazi et al., 2012). On the other hand, the mechanical stability of the crops is influenced by the mechanical strength of soils (Berry et al., 2003; 2004), which is an important research subject for sustainable cereal production. Cereals have their grains at their upper sides of the body, hence, loss of stability called lodging causes the decline of both the yield and the qualities. For instance, it is reported that severe lodging causes more than 45 % of yield losses (Baker et al., 1998; 2014), and also causes low grain quality due to the delay of the harvest. Since the failure of root-soil systems induces severe and permanent lodging, it is essential to present mathematical and physical models to understand and predict plant-soil interactions to sustain the productivity of cereals.

Vegetation reinforces surface layers on both of artificial soil structures and natural slopes (Bischetti et al., 2010; Liu et al., 2016; Bizet et al., 2018). Rainfall events often cause erosion of soil particles on natural/artificial slopes(Das et al., 2018), which induces geo-disasters of soil structure as dams, embankments, slopes, roads, and other foundations. It is often employed that slope protections by using concrete, cemented soils, and artificial fibers. Although these methodologies substantially increase the resistance of the soil structures, there are annoying problems that the deterioration of concrete, cement, and synthetic fibers induces the reduction of the function. The deterioration also result in increasing the life-cycle costs of soil structures. By contrast, biological reinforcement such as plant roots increases the shear strength of soils (Hejazi et al., 2012) with far less financial costs than the artificial materials since biological materials grows and increase the resilience of the soil structures against the erosion. The reinforcement is relatively weak and hard to predict quantitatively. Therefore, the utilization of biological reinforcement is still less common than artificial ones.

From another standpoint, soil supports crops to prevent lodging. Lodging is defined as a permanent displacement of cereals (Baker et al., 1998) and induced by loss of stability of plant body and rhizosphere. Prevention of lodging is one of the most critical problems to sustain yield and quality of cereals (Baker et al., 1998; Berry et al., 2004) since the lodging causes pre-harvest sprouting, diseases, and decline of the radiation utilization efficiency. There are two types of lodging: stem lodging and root lodging. Stem lodging is caused by bending or breakage of plant stems, and there has been presented that some schemes to estimate and prevent this type of lodging (Ookawa et al., 2010). The root lodging, however, is still hard to predict, and the prediction/prevention is being challenged. Beker et al. (1998) proposed a method to predict the root lodging of wheat, which is an empirical model based on numerous observation data from field experiments. Though Baker's model is convenient for roughly simulating the lodging of wheat, it has difficulty for its accuracy when it is used for breeding or field management. To increase the accuracy of the lodging model, it is necessary to propose physics-based methods such as numerical simulations for plant-soil systems.

The problems mentioned above motivate researchers to investigate and predict plant-soil mechanical interactions for decades. it has been presented that roots reinforce the rooted soils, and the reinforcement is visible as incremental cohesion/friction. The reinforcement model has been utilized for the homogeneous approach which models rooted soils as homogeneous domain. In the 1990s, Abe and Ziemer (1990) propose a method to estimate the shear strength of the rooted soils from material properties and geometries of roots and soils. The Mohr-Coulomb model is one of the most widely-used models to estimate the stability of rooted soils in artificial/natural slopes (Rahardjo et al., 2009; Rahardjo et al., 2014; Eab et al., 2015; Zhu et al., 2017).

Recently, Dupuy et al. (2007; 2018) and Michovski et al. (2011) propose direct simulations of root-soil contact problems based on the Finite Element Method (FEM) and simple root-soil contact models. They utilize commercial software packages of the FEM with some mechanical data of plants, soils, and root-soil interfaces to directly predict the deformation of roots, soils, and contact between roots and soils. These approaches are substantially innovative since the methods can utilize the exact root morphology in the prediction, which has not been done in the previous approaches. Their approach clearly visualizes the stress fields of the soils and roots, which provides far more detailed information to estimate and understand the deformation of rooted soils. For instance, Dupuy's approach gives a prediction of the failure zone of roots and soils and shows how wind forces are propagated from roots to soils, which did not estimate by the conventional approaches based on the Mohr-Coulomb model.

Although the direct approaches are novel and accurate, some important problems are still remained about the constitutive model of root-soil contact interfaces to utilize the models for practical problems such as soil erosions and lodging. The primary problem is the absence of a consistent method to measure the shear strength of root-soil interfaces. The FEM with contact models necessitates slip criterion of root-soil interfaces which express cohesion and frictions. However, there have not been presented any methods which accurately measure cohesion and friction of root-soil interfaces.

Further, another problem exists for the discretization scheme of the root-soil interfaces. Dupuy et al. (2007) utilized the Node-To-Node (NTN) approach, which does not allow slip of the interface, and Michovski et al. (2011) used the Line Element (LE) approach which requires special conversion from 2-D or 3-D scanned data to straight or curved lines. Therefore, to utilize the direct simulation of root-soil contact problems for the design and management of the soil structures and crops, it is necessary to develop both of discretization scheme of root-soil interfaces and software to predict the root-soil contact problems.

This thesis aims to present a set of experiments, constitutive models, and numerical methods for predicting the deformation of rooted soils based on the computational contact mechanics (Hughes et al., 1976;) approach with FEM. As discussed in the previous subsection, numerical simulations of root-soil contact problem necessitate accurate measurements of shear strength of root-soil interfaces such as frictional coefficient of

root-soil interface, and cohesion induced by suction. However, little experiments are available for measuring frictional coefficients of root-soil interfaces, and no models are presented to obtain cohesion in root-soil interfaces induced by suction. This thesis presents two novel experiments to measure friction and suction-induced cohesion, respectively. From these experiments, two models that are utilized for soil-soil interfaces are introduced to give mathematical expressions for friction (Mohr-Coulomb model) and suction-induced cohesion (Vilar model, Vilar, 2006), which are implemented for numerical simulations of root-soil contact problems. It is also discussed in the previous subsection that NTN and LE approaches have limitations for expressing such root-soil contact phenomena as (1) slip between roots and soils, (2) separation between roots and soils, or (3) complex root geometry and surface topology of root-soil interfaces. These limitations result in reduced accuracy or high pre-processing costs in the previous results. The Node-To-Segment (NTS) approach which is a modified approach of the NTN, hence, is newly introduced in the thesis to avoid these problems, which can express (1) slip between roots and soils under large-slip conditions, (2) separation/contact between roots and soils, and (3) geometrical nonlinearity of roots and soils. Although the original version of the NTS approach induces ill-convergence problems when it is applied for root-soil contact problems (Dupuy et al., 2008), a novel scheme is successfully introduced to stabilize the NTS approach. The following chapters are devoted to the set of experiments, modeling, and numerical simulations.

In Chapter 2, the outline of the NTS approach with FEM (NTS-FEM) is briefly explained to model root-soil contact interfaces. The chapter presents kinematics of root-soil contact problems, mathematical expressions of the governing equation, the discretization and linearization of the governing equation, and the solution algorithm for numerical simulations. Since the solution algorithm for the numerical simulation necessitates the constitutive modeling of roots, soils, and root-soil interfaces, the chapter also discusses experiments and models for the mechanical characteristics of them.

Chapter 3 proposes a novel pull-out apparatus to measure the cohesion and frictional coefficient of root-soil interfaces, both of which are essential to perform root-soil contact simulations. The pull-out apparatus is validated by measuring the frictional coefficient of a steel-sand interface, which has been measured in previous studies (Uesugi and Kishida., 1986). It is also confirmed that shear zones in experiments are not mainly in the roots or soils, but the root-soil interface through the comparison between the steel-sand tests and the wood-sand tests. Afterward, the shear strength of root-soil interfaces is measured by using a paddy soil, and the apparatus accurately measure a root of barley, which suggests that the Mohr-Coulomb (MC) model well governs the shear stress of root-soil interfaces as well as the frictional coefficients and the cohesion.

Chapter 4 presents a 2-D experiment and a numerical simulation of the lodging problem, which utilizes the apparatus presented in the previous chapter. The chapter contains the implementation of the NTS approach, a novel stabilization scheme of the NTS approach, and the procedure to measure the material parameters of roots, soils, and root-soil interfaces. The chapter also contains numerical simulations for pull-out tests and lodging problems to validate and confirm the accuracy of the present method. The results are highly consistent with both of the experiments and suggested that the present method is capable of reproducing the deformation of rooted soils.

Chapter 5 describes a set of methods to measure, model, and predict the shear strength of root-soil contact interfaces under dynamic suction conditions, the model of which is based on Mohr-Coulomb-Vilar (MCV) model with the NTS approach. The chapter extends the MC model to predict the shear strength of root-soil interfaces under dynamic suction conditions.

Chapter 6 shows validations and applications of the root-soil contact simulation based on the MCV model. The MCV model is first validated by simulating the suction-controlled pull-out tests and then applied for a numerical experiment of pull-out tests under dynamic suction conditions. The results show that the MCV-NTS approach expresses the root-soil contact behavior under dynamic suction conditions. The numerical experiment of the pull-out behavior of roots is performed, and the effect of wet-dry conditions is reasonably

estimated as the pull-out force of roots.

Chapter 7 remarks on the conclusion of the whole thesis and describes future studies.

2 Continuum Model for Root-Soil Contact Problem

This section summarizes general formulations for frictional-cohesion contact problems. First, the contact kinematics is described where the schematics of the contact problem and mathematical expression of the deformation and contact, stick, and slip are given based on the CCM. Second, it is also shown that the weak form of contact problems in terms of FEM and the NTS approach. Afterward, the discretization and matrix form of domains and contact surfaces are explained in which friction and cohesion are also modeled and discretized by using contact elements. Lastly, the solution algorithm is discussed.

2.1 Formulation of root-soil contact interface

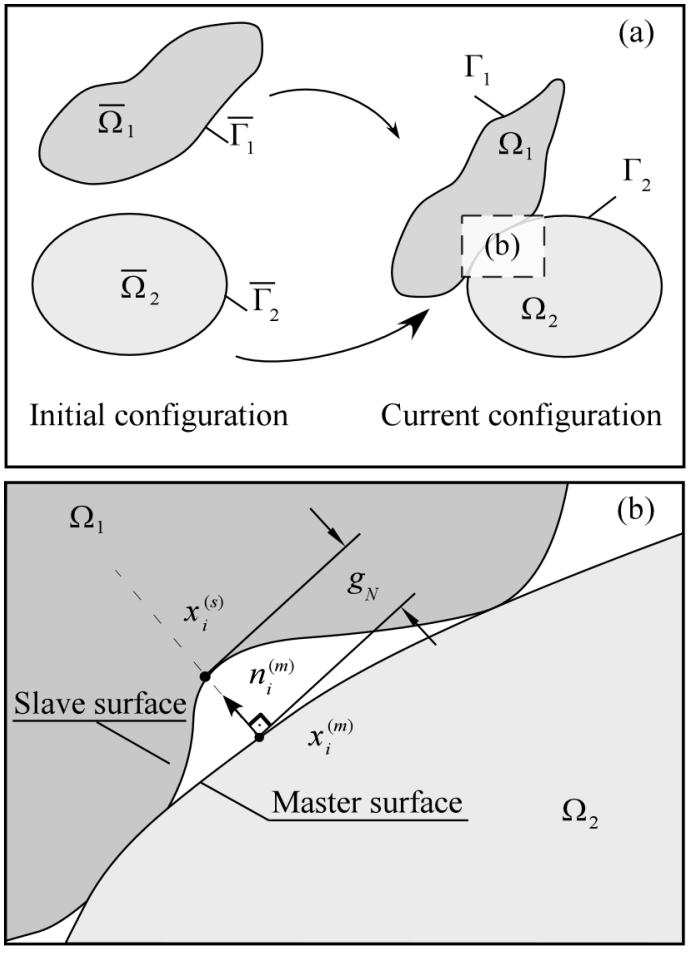

Figure 1: Schematic view of contact kinematics.

This section reviews the contact kinematics and its formulation in terms of CCM. The formulation of

roots and soils were done by using the finite elasto-plasticity and the CCM. This section summarizes the derivation of the governing equation of contact problems and its discretization by using the NTS approach (Wrigger, 2006). Let us consider two deformable bodies, in which one is usually denoted as the master body $\left(\Omega_1, \overline{\Omega}_1\right)$ and another as the slave body $\left(\Omega_2, \overline{\Omega}_2\right)$. Both bodies can undergo deformation through motion during $[0, t]$ and come into contact, where (Ω_1, Ω_2) is identified at the current configuration and $\left(\overline{\Omega}_1, \overline{\Omega}_2\right)$ is in the initial configuration (Fig. 1). Further, in the current configuration, boundaries of each body can be divided into three non-overlapping subdivisions: displacement boundaries, traction boundaries, and contact boundaries.

Accordingly, the governing equation for the displacement field is given by a virtual work equation,

$$\begin{aligned} \delta W = &\left(\int_\Omega \sigma_{ij} \frac{\partial \delta u_i}{\partial x_j} d\Omega - \int_\Omega f_i \delta u_i d\Omega - \int_\Gamma t_i \delta u_i d\Gamma \right)^m \\ &+ \left(\int_\Omega \sigma_{ij} \frac{\partial \delta u_i}{\partial x_j} d\Omega - \int_\Omega f_i \delta u_i d\Omega - \int_\Gamma t_i \delta u_i d\Gamma \right)^s + \delta W^c = 0, \end{aligned} \tag{1}$$

where i and j are subscripts which have values of 1, 2, 3 in the three-dimensional Euclidean space, δW is the virtual work, superscripts m and s denote the master/slave notations in the current configuration, Γ is the boundary of the domains, σ_{ij} is the Cauchy stress tensor, δu_i is the virtual displacement vector, δ is the variational operator with respect to displacement, f_i is the body force vector, and t_i is the traction vector. The first and second terms are identical to the conventional virtual work for one-body problems (Hashiguchi and Yamakawa, 2013). The last term represents the virtual work for the contact interfaces, which is derived from the constraint conditions such as the non-penetration conditions, friction, and cohesion (Wriggers, 2006). The virtual work of contact interfaces δW^c is generally taking the form of

$$\delta W^c = \int_\Gamma t_{Ni} \delta g_{Ni} d\Gamma + \int_\Gamma t_{Ti} \delta g_{Ti} d\Gamma, \tag{2}$$

in which t_{Ni} and t_{Ti} are the normal and the frictional stress, respectively. g_{Ni} is the normal gap and g_{Ni} is the tangential displacement from the initial contact point (Fig. 1). Here, the first term enforces the normal contact stress to prevent overlaps between the bodies, and the second term works as the tangential one such as friction and cohesion. This interfacial virtual work δW^c is analogous to the well-known virtual work, and it becomes zero under contactless conditions (Wriggers, 2006).

The first and the second term of the governing equation (Eq. (1)) are discretized by using the finite elements, and the last one is discretized by using the NTS elements. The bodies are initially discretized by finite elements, as illustrated in Fig. 1. Then, each node on the slave surface is paired with the closest segment on the master surface (Fig. 2). Since the contact element mechanically connects a node to a segment, it is called an NTS element. From the geometrical relationship, the normal gap vector g_{Ni}, tangential gap vector g_{Ti} is formulated by using the nodal coordinates. Under the penalty method, a slave node and a master segment are connected by virtual springs, as depicted in Fig. 2 (b) and (c), which is the penalty parameter. The frictional stress is relaxed if it is greater than the frictional strength, which is described as the parallel shift of the virtual spring from the initial contact point (Fig. 2). Above all, the governing equation is given by

$$\delta W_c = \sum_{A=1}^{ne} \delta {u_i}^{d(A)} {R_i}^{d(A)} + \sum_{A=1}^{nc} \delta {u_i}^{c(A)} {R_i}^{c(A)} \tag{3}$$

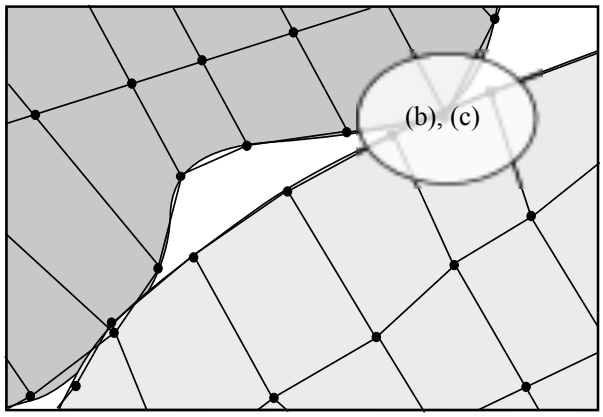

(a)

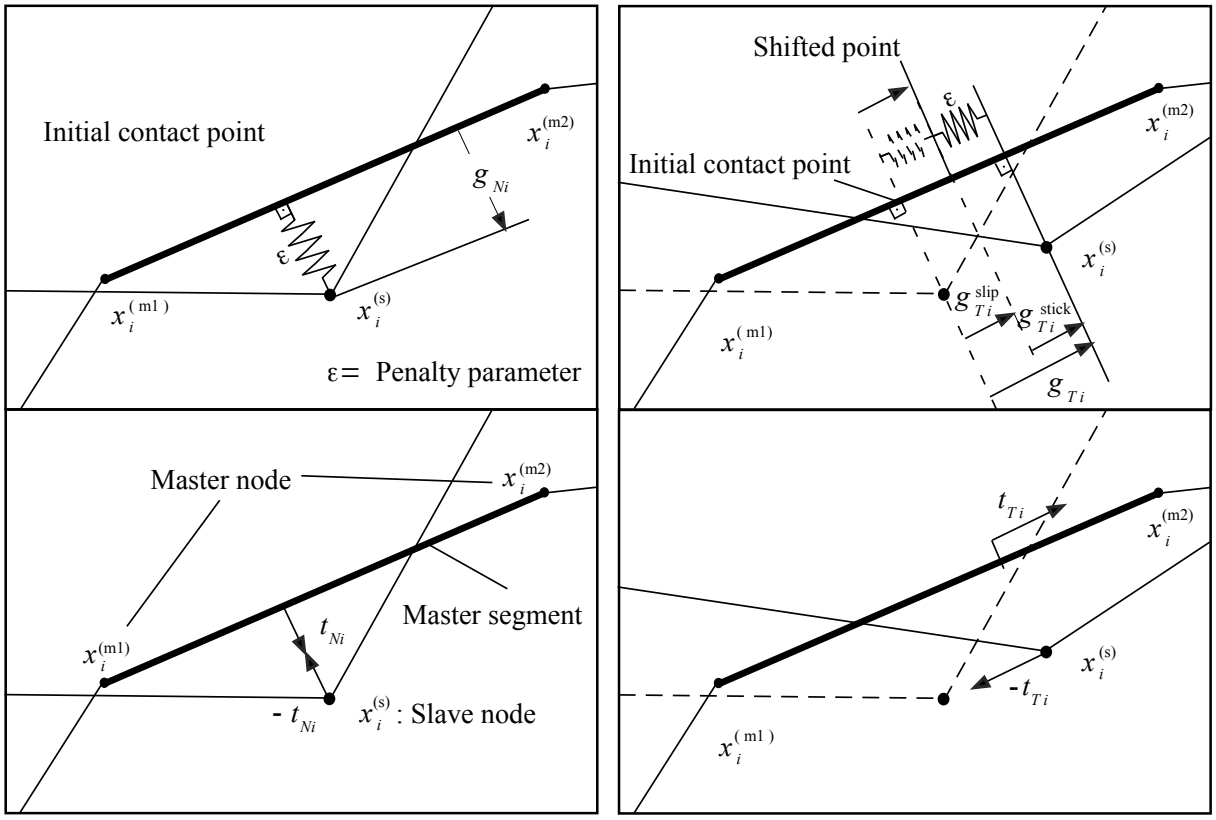

(b) (c)

Figure 2: Schematic view of NTS contact elements with the penalty method. (a) Contact interfaces formed between two finite element meshes, (b) expression of normal contact, and (c) model of stick-slip phenomenon in terms of the NTS approach.

where A and B denote the identification numbers of nodes in each element, ne and nc are the numbers of finite elements and NTS elements, respectively, $\delta {u_i}^{d(A)}$ and $\delta {u_i}^{c(A)}$ are variations of the nodal displacement vectors for the bodies and the contact interfaces, ${R_i}^{d(A)}$ and ${R_i}^{c(A)}$ are the residual vectors. The detailed derivation of the previous equation is displayed in the next section.

This section provides the standard contact algorithm based on the penalty method (Wriggers, 2001; Liu et al., 2006) and an implementation of the friction and the cohesion. For solving the discretized equations (Eq. (2.3)), the Newton's method is utilized since the discretized equations have nonlinear relationships with the displacement (Wriggers et al., 2001; Liu et al. 2003; Wriggers, 2006). From Eq. (3), the linearized equation is expressed by

$$\begin{aligned} \delta W + \frac{\partial (\delta W)}{\partial u_i} \Delta u_i = & \sum_{A=1}^{ne} \sum_{B=1}^{ne} \delta {u_i}^{d(A)} \left({R_i}^{d(A)} + \left[{K_{ij}}^{d(AB)} \right] \Delta {u_i}^{d(B)} \right) \\ & + \sum_{C=1}^{nc} \sum_{D=1}^{ne} \delta {u_i}^{c(C)} \left({R_i}^{c(C)} + \left[{K_{ij}}^{c(CD)} \right] \Delta {u_i}^{c(D)} \right), \end{aligned} \tag{4}$$

in which Δu_i denotes the displacement increments, u_i is the global displacement vector, $\left[{K_{ij}}^{d(AB)} \right]$ is the stiffness matrix of each finite elements, $\left[{K_{ij}}^{c(CD)} \right]$ is the stiffness matrix of contact elements. As the NTS elements share the nodes with the finite elements as seen in Fig. 2, Eq. (4) can be assembled into a system of equation

$$\left[K_{\alpha\beta} \right] \Delta u_\beta = -R_\alpha \tag{5}$$

$$\left[K_{\alpha\beta} \right] = \cup \langle \left[{K_{ij}}^{d(AB)} \right], \left[{K_{ij}}^{c(CD)} \right] \rangle \tag{6}$$

$$R_\alpha = \cup \langle {R_i}^{d(A)}, {R_i}^{c(C)} \rangle \tag{7}$$

where $\left[K_{\alpha\beta} \right]$ is the global stiffness matrix, R_α is the global residual vector, and $\cup\langle \cdot, \cdot \rangle$ is the matrix-vector assembly operator, which rearrange a matrix form into a vector form. In every iteration in the Newton's method, the displacement fields are updated by using the solution of Eqs. (5), (6), and (7).

For the sake of stability of the solution algorithm, there are two phases during every time step, which are the first and the second the Newton's loop (Wriggers, 2006). The first Newton's loop is in the trial mode, in which the frictional stress assumed to be proportional to the displacement without any plastic slip. After the convergence, the frictional law is enforced in the second phase, where displacement and frictional stress are updated at every iteration until equilibrium is achieved.

In order to update frictional stress (Fig. 2), the return-mapping algorithm is employed. The algorithm is originally proposed by Simo and Taylor (1986) for updating stress in the framework of the elasto-plasticity. The idea has been extended in terms of the CCM as an algorithm for updating the frictional stress (Peric and Owen, 1992; Wriggers et al., 2001). Although the scheme generally is solved by iterative methods, it can be directly solved in case of the Mohr-Coulomb's model,

$$f = \sqrt{t_{Ti} t_{Ti}} - \mu \cdot \epsilon \sqrt{g_{Ni} g_{Ni}} - c \geq 0 \tag{8}$$

where f is the yield function, μ is the frictional coefficient and c is the cohesion. The system of equations is given by,

$$t_{Ti}^{n+1} = \epsilon \left(g_{Ti}^{n+1} - \mathbf{g}_{Ti}^{slip,n+1} \right) (f > 0) \tag{9}$$

$$t_{Ti}^{n+1} = \left(\mu \sqrt{t_{Ni}^{n+1} t_{Ni}^{n+1}} + c \right) \frac{t_{Ti}^{tr,n+1}}{\sqrt{t_{Ti}^{tr,n+1} t_{Ti}^{tr,n+1}}} \tag{10}$$

$$g_{Ti}^{slip,n+1} = g_{Ti}^{slip,n} \, (f < 0) \tag{11}$$

$$g_{Ti}^{slip,n+1} = g_{Ti}^{slip,n} + \frac{\left(\sqrt{t_{Ti}^{n+1} t_{Ti}^{n+1}} - \mu \cdot \sqrt{t_{Ni}^{n+1} t_{Ni}^{n+1}} - c \right)}{\epsilon} \cdot \frac{t_{Ti}^{tr,n+1}}{\sqrt{t_{Ti}^{tr,n+1} t_{Ti}^{tr,n+1}}} \, (f \geq 0) \tag{12}$$

where $t_{Ti}^{tr,n+1}$ is the frictional trial stress, and these equations are used in the solution algorithm.

In this thesis, a simple modification is proposed for the pairing algorithm of the NTS element, which is explained in detail in Chapter 4. One of the main issues in the NTS formulation is that the pairing between a node and a segment is not unique in some cases (Wriggers, 2006; Zavarise and De Lorenzis, 2009). For instance, there are two possible master segments for single slave node. This phenomenon causes oscillations of the solution and the ill-convergence problem (Zavarise and De Lorenzis, 2009). Extensive research has shown that the problem is avoided by introducing a smooth surface in interfaces. Wriggers et al. (2001) have proposed some interpolations by using the Hermite functions and the cubic Bernstein functions. A more straightforward method has been proposed by Liu et al. (2003). However, these approaches are far more complicated than the original NTS approach due to the nonlinearity of the interpolations. Therefore, in this thesis, a simple algorithm is provided to avoid this problem, as illustrated in Chapter 4, and it is illustrated that the algorithm increases the robustness.

2.2 Formulations of root and soil

This section presents the discretization of domains, where two following points are discussed based on the NTS approach. First, the virtual work should be formulated in terms of the current configuration since the momentum balance can be formulated only at the current configuration, and not in the initial configuration within contact problems (Wriggers, 2006). Also, a constitutive equation used in the formulation should satisfy objectivity for rotation. The reason for it is that the frictional contact problem, as presented here, is large-deformation or large-slip problems where domains significantly rotate. A formulation is based on the finite strain theory with the multiplicative decomposition of the deformation gradient tensor to satisfy the objectivity.

The finite strain theory is derived from the momentum balance in the current configuration,

$$\frac{\partial \sigma_{ij}}{\partial x_j} + \rho b_i = \rho \dot{v}_i \tag{13}$$

where σ_{ij} is the Cauchy stress tensor, v_i the velocity and $\dot{v}_i$ the acceleration, b_i is the body force, ρ is the bulk density, x_j is the coordinate in terms of current configuration. Eq. (13) is solved with Dirichlet boundary condition (displacement boundary)

$$u_i = \bar{u}_i \quad \text{on} \quad \Gamma_u, \tag{14}$$

Neumann boundary condition (traction boundary condition)

$$\sigma_{ij} n_j = \bar{t}_i \quad \text{on} \quad \Gamma_t, \tag{15}$$

and initial conditions

$$u_i = \bar{u}_i \quad \text{on} \quad t = 0, \tag{16}$$

$$\sigma_{ij} = \bar{\sigma_{ij}} \quad \text{on} \quad t = 0, \tag{17}$$

where Γ_u is the Dirichlet boundary and $\bar{u}_i$ is the displacement on the boundary, Γ_t is the Neumann boundary and $\bar{t}_i$ is the traction on the boundary, n_j is the normal vector on the boundary, $\bar{u}_i$ and $\bar{\sigma_{ij}}$ are initial values. Consequently, the integral form of Eq. (13) is

$$\int_\Omega \frac{\partial \sigma_{ij}}{\partial x_j} d\Omega + \int_\Omega \rho b_i d\Omega = \int_\Omega \rho \dot{v}_i d\Omega \tag{18}$$

In case of the formulation based on finite strain theory, Eq. (13) and above initial/boundary conditions are pulled back to the initial configuration for convenience. Among the various pull-back operations, following pull-back operation is often used,

$$P_{iJ} = \tau_{ik} F^{-T}_{kJ} = J \sigma_{ij} F^{-T}_{kJ} \tag{19}$$

where τ_{ik} is the Kirchhoff stress tensor, P_{iJ} is the first Piola-Kirchhoff stress tensor, F_{iJ} is the deformation gradient tensor which is the two-point tensor and explained in detail in the next section,

$$F_{iJ} = \frac{\partial x_i}{\partial X_J} \tag{20}$$

where X_J is the coordinate of initial configuration and J is

$$J = \epsilon_{IJK} F_{1I} F_{2J} F_{3K} \tag{21}$$

where ϵ_{IJK} is the Levi Civita symbol.

Based on this pull-back operation, an area is pulled-back as

$$\sigma_{ij} d\Gamma = \frac{\tau_{ik}}{J} F^{-T}_{kJ} N_J J d\bar{\Gamma} = P_{iJ} N_J d\bar{\Gamma} \tag{22}$$

where N_J is the normal vector on the initial configuration. From the relationships, the integral form of the Eq. (13) is pulled back by using the relationship of Eq. (19) as

$$\int_{\bar{\Omega}} \frac{\partial P_{iJ}}{\partial X_J} d\bar{\Omega} + \int_{\bar{\Omega}} \rho_0 b_i d\bar{\Omega} - \int_\Omega \rho_0 \dot{v}_i d\bar{\Omega} = 0 \tag{23}$$

where $\bar{\Omega}$ and $\bar{\Gamma}$ are the domain and the surface in terms of the initial configuration, respectively, and ρ_0 is the density with respect to the initial configuration. Taking the weak derivative of the equation, the weak form is obtained.

$$
\begin{aligned}
\delta W^d &= \int_{\bar{\Omega}} \frac{\partial P_{iJ}}{\partial X_J} \delta u_i d\bar{\Omega} + \int_{\bar{\Omega}} \rho_0 b_i d\delta u_i \bar{\Omega} - \int_{\Omega} \rho_0 \dot{v}_i \delta u_i d\bar{\Omega} \\
&= \int_{\bar{\Omega}} P_{iJ} \frac{\partial \delta u_i}{\partial X_J} d\bar{\Omega} + \int_{\bar{\Omega}} \rho_0 b_i d\delta u_i \bar{\Omega} - \int_{\Omega} \rho_0 \dot{v}_i \delta u_i d\bar{\Omega} - \int_{\bar{\Gamma}} \bar{t}_i \delta u_i d\bar{\Gamma} \\
&= 0
\end{aligned} \tag{24}
$$

where δW^d is the virtual work of domains.

Since Eq. (24) is a system of nonlinear equations, it is solved by the Newton's method. The linearized equation is analytically computed by taking the directional derivative of δW for displacement field u in terms of the initial configuration. The linearized equation is given below. The first term of the right-hand side part is discretized by following mathematical operations. First, let us linearize the Eq. (24).

$$
\frac{\partial \delta W^d}{\partial X_I} \Delta u_I = \frac{\partial}{\partial X_I} \int_{\bar{\Omega}} P_{iJ} \frac{\partial \delta u_i}{\partial X_J} d\bar{\Omega} \Delta u_I \tag{25}
$$

Here, the first Piola-Kirchhoff stress tensor has the relationship of $P_{iJ} = F_{iK} S_{KJ}$. Substituting this to the Eq. (26),

$$
\frac{\partial \delta W^d}{\partial X_I} \Delta u_I = \int_{\bar{\Omega}} \frac{\partial F_{iK} S_{KJ}}{\partial X_I} \Delta u_I \frac{\partial \delta u_i}{\partial X_J} d\bar{\Omega} \tag{26}
$$

noting that the directional derivative is decomposed as

$$
\frac{\partial F_{iK} S_{KJ}}{\partial X_I} \Delta u_I = \frac{\partial F_{iK}}{\partial X_I} S_{KJ} \Delta u_I + F_{iK} \frac{\partial S_{KJ}}{\partial X_I} \Delta u_I \tag{27}
$$

with

$$
\frac{\partial F_{iK}}{\partial X_I} S_{KJ} \Delta u_I = \frac{\partial \Delta u_I}{\partial X_J} S_{KJ}, \tag{28}
$$

and

$$
F_{iK} \frac{\partial S_{KJ}}{\partial X_I} \Delta u_I \delta u_i \partial X_J = \delta E_{IJ} C_{IJKL} \Delta E_{KL}. \tag{29}
$$

Substituting Eqs (27) to (29) into Eq. (26), Eq. (30) is obtained.

$$
\frac{\partial \delta W^d}{\partial X_I} \Delta u_I = \int_{\bar{\Omega}} \left(\frac{\partial \Delta u_I}{\partial X_J} S_{JK} \frac{\partial \delta u_I}{\partial X_K} + \delta E_{IJ} C_{IJKL} \Delta E_{KL} \right) d\bar{\Omega} \tag{30}
$$

where C_{IJKL} is the algorithmic stiffness matrix in terms of reference configuration since the contact can only be described with respect to the current configuration. Eq. (30) is pushed-forward to the current configuration.

$$
\frac{\partial \delta W^d}{\partial X_I} \Delta u_I = \int_{\Omega} \left(\frac{\partial \Delta u_i}{\partial x_j} \sigma_{jk} \frac{\partial \delta u_i}{\partial x_k} + \delta d_{ij} \bar{c}_{ijkl} \Delta d_{kl} \right) d\Omega \tag{31}
$$

where $\bar{c}_{ijkl}$ is the stiffness matrix with respect to the current configuration,

$$
\bar{c}_{ijkl} = \frac{1}{J} F_{iI} F_{jJ} F_{kK} F_{lL} \bar{C}_{IJKL} \tag{32}
$$

Eq. (31) is discretized based on Galerkin's method, thereby, the stiffness matrix $K^{d(IJ)}$ of Eq. (4) is obtained.

$$K^{d(IJ)} = K_1^{d(IJ)} + K_2^{d(IJ)} \tag{33}$$

where $K_1^{d(IJ)}$ and $K_2^{d(IJ)}$ are

$$K_1^{d(IJ)} = \int_{\Omega_e} \frac{\partial N_I}{\partial x_k} \tau_{kl} \frac{\partial N_J}{\partial x_l} d\Omega_e \tag{34}$$

$$K_2^{d(IJ)} = \int_{\Omega_e} B_{Ik} D_{kl} B_{lJ} d\Omega_e \tag{35}$$

since the Eq. (36) is discretized as below.

$$\frac{\partial \delta W^d}{\partial X_I} \Delta u_I = \int_{\Omega_e} \left(\delta u_I \frac{\partial N_I}{\partial x_k} \tau_{kl} \frac{\partial N_J}{\partial x_l} \Delta u_J + \delta u_I B_{Ik} D_{kl} B_{lJ} \Delta u_J \right) d\Omega_e \tag{36}$$

2.3 Solution algorithm

This subsection discusses the solution algorithm for root-soil contact simulations. As discussed in the last subsection, the system of equations is nonlinear with respect to the displacement field. Consequently, iterative solver such as the Newton's method is to be employed, where the trial variables of displacement and internal variables (e.g., stress measure, strain measure, and softening/hardening parameters) are updated so that the final solution satisfies the virtual work equation (Eq. (24)) and the yield criterions of domains and interfaces. The solution algorithm also updates the pairing of contact elements (Fig. 2) within the iterative loops of the Newton's method; this pairings algorithm is also explained in the current subsection.

Chapters 4 and 5 show solution algorithms for friction-cohesion contact problems. The algorithm consists of two parts: a stick part and a slip part. In the stick part, all contact elements are under elastic stick conditions, which indicates no slip is allowed in the interfaces. The stress, internal variables, and displacements are computed as trial values, which are used as the initial trial value of the second part. The second part, afterward, updates the frictional stress where the slip is allowed. The scheme mentioned above is a widely-used technique to reduce the instability of the iterative method, as shown in Wriggers (2006). In each part, the pairing is detected firstly, and then the stiffness matrix and residuals are computed for every solid and contact elements. Then some linear solver is utilized to solve the system of discretized equations, for instance, the iterative method as the Conjugate Gradient (CG) method or direct solver such as the Gauss-Jordan method.

The configurations of domains and contact interfaces are updated based on the stress-updating methods, as seen in the previous subsections. The stress, plastic strain measure, and hardening/softening parameters are updated based on elasto-plasticity, and the shear stress of root-soil interfaces is updated by the stress-updating scheme discussed in Eq. (12).

3 Constitutive model and material tests of root and soil domains

This section discusses material tests and modeling of the root matrix in terms of continuum mechanics and CCM. The present model based on the CCM necessitates some parameters to solve the system of equations. The parameters are roughly categorized into the material parameters for root domains, soil domains, and ones of root-soil interfaces. This section discusses the physical tests and models for domains of roots and soils, and the next section describes that for root-soil interfaces. The material tests of roots are not

standardized; therefore, this section proposes a possible simplest method and an apparatus to measure the stiffness parameters of roots. As for the material tests of soils, there have been many methods to determine the stiffness parameters, and the method is standardized by, for instance, the JIS and the JGS. Thereby the present section introduces some of the testing methods to measure the stiffness parameters of soils from the standardized methods. The constitutive models for roots and soils are also to be discussed. For these reasons, the current section utilizes some consistent models for roots and soils.

This section firstly provides a summary of the finite strain theory for general cases which include both elastic and plastic behaviors. From the standpoint of finite strain theory, the constitutive model is given as an elastic/plastic potential function; consequently, this section also suggests the possible simplest models of both potential functions.

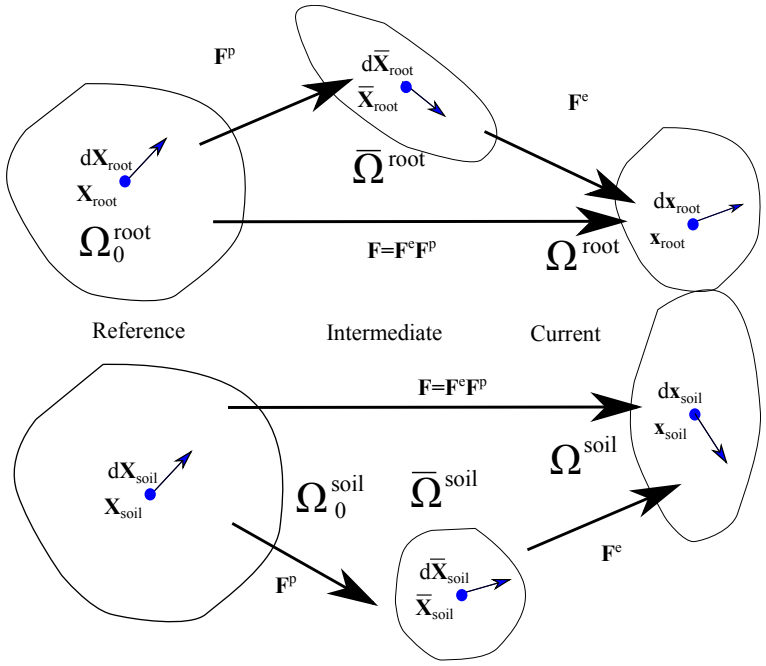

Figure 3: Schematic view of kinematics of two elasto-plastic bodies and the kinematic measures.

The contact kinematics with the finite strain theory is shown in Fig. 3, whereas the reference configurations Ω_0^{root}, Ω_0^{soil}, and the current configurations Ω^{root}, Ω^{soil} indicate the initial and present control volumes, respectively. Hereby the intermediate configurations $\bar{\Omega}^{root}$, $\bar{\Omega}^{soil}$ are also introduced to describe the virtual stress-free configuration. It is worth noting that the stress-free configuration is purely virtual and not uniquely observed in realistic situations and introduced just for convenience. Thanks to the stress-free intermediate configurations, the constitutive models of elastic/plastic parts are simply expressed as below by using elastic/plastic potential functions, respectively. Under these assumptions, let us project a small vector around a material point in terms of the reference configuration, which is denoted as dX_I into the intermediate/current configurations as shown in the figure, where the superscript ^{root} and ^{soil} denote the amounts of the roots and soils, respectively; the projections are visible as $d\bar{X}_I$ and dx_i. Further, the deformation gradient tensor is introduced as follows;

$$dx_i = \frac{\partial x_i}{\partial X_J} dX_J = F_{iJ} dX_J \tag{37}$$

$$dx_i = \frac{\partial x_i}{\partial \bar{X}_{\bar{J}}} d\bar{X}_{\bar{J}} = F_{i\bar{J}}{}^{e} d\bar{X}_{\bar{J}} \tag{38}$$

$$d\bar{X}_{\bar{I}} = \frac{\partial \bar{X}_{\bar{J}}}{\partial X_J} dX_J = F_{\bar{I}J}{}^{p} dX_J \tag{39}$$

where F_{iJ} is the deformation gradient tensor, $F_{i\bar{J}}{}^{e}$ is the elastic deformation gradient tensor, and $F_{\bar{I}J}{}^{p}$ is the plastic deformation gradient tensor (e.g. Hashiguchi and Yamakawa, 2013). Hence, the three deformation gradient tensors has a relationship of Eq. (40)

$$F_{iJ} = \frac{\partial x_i}{\partial X_J} = \frac{\partial x_i}{\partial \bar{X}_{\bar{I}}} \frac{\partial \bar{X}_{\bar{I}}}{\partial X_J} = F_{i\bar{I}}{}^{e} F_{\bar{I}J}{}^{p}. \tag{40}$$

As well as vectors, areas and volumes are projected and the mathematical expression of the projections are also given by using deformation gradient tensors. First, areas are projected by

$$da_i = n_i da = JF_{iJ}{}^{-T} N_J dA = JF_{iJ}{}^{-T} dA_J \tag{41}$$

where n_i and N_J are the outer normals with respect to the infinitesimal area, which is called the Nanson's formula. The analogous of the Nanson's formula is also given for other two projections for elastic and plastic deformation gradient tensors.

$$da_i = n_i da = J^e F_{i\bar{I}}{}^{e-T} \bar{N}_{\bar{I}} d\bar{A} = JF_{i\bar{I}}{}^{e-T} d\bar{A}_{\bar{I}} \tag{42}$$

$$d\bar{A}_{\bar{I}} = \bar{N}_{\bar{I}} d\bar{A} = J^p F^{p-T}_{\bar{I}J} N_J dA = J^p F_{\bar{I}J}{}^{p-T} dA_J, \tag{43}$$

where da_i, $d\bar{A}_{\bar{I}}$, and $d\bar{A}_I$ are the area vectors on the current, the intermediate, and the initial configuration, respectively. $\bar{N}_{\bar{I}}$ is the normal vector on the area in the intermediate configuration. The projection of the volumes are described as below.

$$dv = JdV = J^e d\bar{V} = J^e J^p dV \tag{44}$$

where $J^e = \epsilon_{I\bar{J}K} F_{\bar{I}}{}^{e} F_{\bar{J}}{}^{e} F_{\bar{K}}{}^{e}$, and $J^p = \epsilon_{IJK} F_I{}^{p} F_J{}^{p} F_K{}^{p}$

The elastic constitutive equations are provided by using the elastic deformation gradient tensor $F_{i\bar{I}}{}^{e}$ and decoupled from the plastic deformation gradient tensor $F_{\bar{I}J}{}^{p}$. Before describing the elastic potential function and constitutive models of roots and soils, both strain and stress measures are to be defined. Here are the strain measures which is directly computed by using these deformation gradient tensors.

$$C_{IJ} = F_{Ii}{}^{T} F_{iJ} \tag{45}$$

$$C_{\bar{I}\bar{J}}{}^{e} = F_{\bar{I}I}{}^{eT} F_{I\bar{J}}{}^{e} \tag{46}$$

$$C_{IJ}{}^{p} = F_{I\bar{I}}{}^{pT} F_{\bar{I}J}{}^{p} \tag{47}$$

where C_{IJ} is called right Cauchy-Green tensor, ${C_{\bar{I}\bar{J}}}^{e}$ is called elastic right Cauchy-Green tensor, and ${C_{IJ}}^{p}$ is called plastic right Cauchy-Green tensor. It is worth noting that the elastic right Cauchy-Green tensor ${C_{\bar{I}\bar{J}}}^{e}$ is defined in the intermediate configuration and the others are defined in the reference configuration. Since the elastic right Cauchy-Green tensor is defined in the intermediate configuration, the elastic potential energy and constitutive models are defined in the intermediate configuration. Further, material-time derivative of the strain measures are necessary for the time-integration of the plastic strain measure, for instance, ${C_{IJ}}^{p}$, which is given as analogy of the velocity gradient tensor l_{ij},

$$l_{ij} = \frac{\partial v_i}{\partial x_j} = F_{iK} {F_{Kj}}^{-1} \tag{48}$$

and given as

$$\bar{L}^{p}_{\bar{I}\bar{J}} = F^{p}_{\bar{I}k} F^{p-1}_{k\bar{J}} \tag{49}$$

where $\bar{L}^{p}_{\bar{I}\bar{J}}$ is the plastic velocity gradient tensor. The symmetric part of this tensor is utilized for plastic flow rule.

$$\bar{D}^{p}_{\bar{I}\bar{J}} = \bar{L}^{p}_{\bar{I}\bar{J}} + {L_{\bar{I}\bar{J}}}^{pT} \tag{50}$$

where $\bar{D}^{p}_{\bar{I}\bar{J}}$ is the plastic stretch tensor.

The work-conjugate stress tensor of the elastic right Cauchy-Green tensor is the Mandel stress tensor, which is given by push-forward of the second Piola-Kirchhoff stress tensor from the initial configuration to the intermediate configuration and pull-back of the Kirchhoff stress tensor $\tau_{ij} = J\sigma_{ij}$ from the current configuration to the intermediate configuration.

$$\bar{M}_{\bar{I}\bar{J}} = {F_{\bar{I}K}}^{p-T} C_{KL} S_{LM} {F_{M\bar{J}}}^{pT} = {F_{\bar{I}k}}^{eT} \tau_{kl} {F_{l\bar{J}}}^{e-T} \tag{51}$$

noting following work-conjugacy.

$$\tau_{ij} : l_{ij} = \bar{M}_{\bar{I}\bar{J}} : \bar{L}_{\bar{I}\bar{J}} \tag{52}$$

Finally, elastic potential functions W, which is equivalent to the Gibbs free energy, are given as function of elastic right Cauchy-Green tensor and satisfy the following relationships.

$$\bar{M}_{\bar{I}\bar{J}} = 2\bar{C}^{e}_{\bar{I}\bar{K}} \frac{\partial W}{\partial \bar{C}^{e}_{\bar{I}\bar{J}}} \tag{53}$$

On the other hand, plastic potential functions and yield functions are defined in terms of Mandel stress tensor $\bar{M}_{\bar{I}\bar{J}}$. For instance, soil constitutive models often utilizes the Drucker-Prager model or Mohr-Coulomb model as their plastic potential function and/or yield functions (Wu et al., 2017): Both models are modeled in Eqs. (54) and (55).

$$f\left(\bar{M}\right)^{Drucker-Prager} = \sqrt{(J_2^{\bar{M}})} + \frac{B_c - 1}{\sqrt{3}B_c + 2\sqrt{3}} I_1^{\bar{M}} - \frac{\sqrt{3}}{B_c + 2} f_c \tag{54}$$

$$f\left(\bar{M}\right)^{Mohr-Coulomb} = \sqrt{(J_2^{\bar{M}})} + \frac{(B_c - 1)\, I_1^{\bar{M}} - 3 f_c}{3\,(B_c + 1)\cos\theta^{\bar{M}} + \sqrt{3}\,(B_c - 1)\sin\theta^{\bar{M}}} \tag{55}$$

where $I_1^{\bar{M}}$, $J_2^{\bar{M}}$, and $\theta^{\bar{M}}$ are the first invariant of the Mandel stress tensor, the second invariant of the deviatoric part of the Mandel stress tensor, and the Lode angle in terms of Mandel stress tensor, respectively. B_c and f_c is computed as below.

$$B_c = \frac{1 + sin\phi}{1 - sin\phi}, \tag{56}$$

where c is the cohesion of soils.

$$f_c = \frac{2ccos\phi}{1 + sin\phi}. \tag{57}$$

The Cauchy stress tensor is often utilized instead of the Mandel stress tensor in case of infinitesimal strain theory. It is worth noting that there is a simple relationship between these invariants of Mandel stress and the Cauchy stress tensors, as seen below. First, the first invariant of the Mandel stress tensor has a relationship of

$$I_1^{\bar{M}} = \bar{M}_{\bar{I}\bar{I}} = JF_{\bar{I}i}^{eT}\sigma_{ij}F_{j\bar{I}}^{e-T} = J\delta_{ji}\sigma_{ij} = J\sigma_{ii} = JI_1^{\sigma}, \tag{58}$$

and the second invariant has a relationship of

$$J_2^{\bar{M}} = \frac{1}{2}\left(\bar{M}_{\bar{I}\bar{J}}\bar{M}_{\bar{I}\bar{J}}\right) = J^2J_2^{\sigma}. \tag{59}$$

Further, the Lode angle of the Mandel stress is the same as the one of the Cauchy stress tensor.

$$\theta^{\bar{M}} = \frac{1}{3}sin^{-1}\left(-\frac{3\sqrt{3}}{2}\frac{J_3^{\bar{M}}}{\left(J_2^{\bar{M}}\right)^{\frac{3}{2}}}\right) = \frac{1}{3}sin^{-1}\left(-\frac{3\sqrt{3}}{2}\frac{J_3^{\sigma}}{\left(J_2^{\sigma}\right)^{\frac{3}{2}}}\right) = \theta^{\sigma} \tag{60}$$

where the third invariants of the deviatoric stress tensor $\bar{M}'_{\bar{I}\bar{J}}$ is defined as seen.

$$J_3^{\bar{M}} = \frac{1}{3}\bar{M}'_{\bar{I}\bar{K}}\bar{M}'_{\bar{K}\bar{L}}\bar{M}'_{\bar{L}\bar{I}} = J^3J_3^{\sigma}. \tag{61}$$

where the deviatoric stress tensor is defined as

$$\bar{M}'_{\bar{I}\bar{J}} = \bar{M}_{\bar{I}\bar{J}} - \frac{1}{\bar{M}_{\bar{K}\bar{K}}}\delta_{\bar{I}\bar{J}} \tag{62}$$

These indicates that the stress invariants are identical with respect to the rotation and only depends upon the volumetric change; this fact is consistent with the definition of the stress invariants. The plastic strain measure, C_{IJ}^p is updated by integrating the increments $\dot{C}_{IJ}^p$ which is computed by flow rule. The flow rule is also described in terms of the intermediate configuration.

$$\bar{D}_{\bar{I}\bar{J}}^p = \Delta\lambda\left(\sqrt{\frac{\partial f}{\partial\bar{M}_{\bar{K}\bar{L}}}\frac{\partial f}{\partial\bar{M}_{\bar{K}\bar{L}}}}\right)^{-1}\frac{\partial f}{\partial\bar{M}_{\bar{I}\bar{J}}} \tag{63}$$

$$\dot{C}_{IJ}^p = 2F_{I\bar{K}}^{pT}\bar{D}_{\bar{K}\bar{L}}^pF_{\bar{L}J}^p = \Xi_{IK}C_{KJ}^p, \tag{64}$$

here, a operator Ξ_{IK} is

$$\Xi_{IK} = 2\Delta\lambda \left(\sqrt{\frac{\partial f}{\partial \bar{M}_{\bar{K}\bar{L}}} \frac{\partial f}{\partial \bar{M}_{\bar{K}\bar{L}}}} \right)^{-1} F^{pT}_{I\bar{K}} \frac{\partial f}{\partial \bar{M}_{\bar{K}\bar{L}}} F^{p-T}_{\bar{L}K}. \tag{65}$$

The plastic strain measure is integrated by using time-integration scheme such as backward-Euler method; the algorithm to compute this time-integration is called the Return-Mapping (RM) method. Here is a general expression of the RM method.

$$Y_{\mu 1} = C^{p}_{n+1,\mu} - \Delta t \Xi_{\mu\nu} C^{np}_{\nu} = 0 \tag{66}$$

$$Y_2 = f^{n+1} = 0 \tag{67}$$

where C^{n+1p}_{μ} and C^{np}_{ν} are the plastic right Cauchy-Green tensors in terms of the time-step $n+1$ and n, respectively. $f^{\bar{M}}_{n+1}$ is a yield function with respect to the Mandel stress tensor. The system of non-linear equations are solved by using the Newton's method.

$$Y^{total,k}_{\mu} = \left(Y^{1,k}_{11}, Y^{1,k}_{12}, \cdots, Y^{1,k}_{33}, Y_{2,k} \right)^{T} = 0 \tag{68}$$

$$X^{total,k}_{\mu} = \left(C^{pn+1,k}_{11}, C^{pn+1,k}_{12}, \cdots, C^{pn+1,k}_{33}, \delta\lambda_k \right)^{T} \tag{69}$$

$$X^{total,k+1}_{\mu} = X^{total,k}_{\mu} - J^{-1}_{\mu\nu} Y^{total,k}_{\nu} \tag{70}$$

where the matrix $J_{\mu\nu}$ is the Jacobian matrix which is updated in every stress-update process in the global solution algorithm. Following subsections present the concrete formulations.

3.1 Constitutive model for root domain

This subsection proposes constitutive models for root domains based on the finite strain theory. In order to determine the constitutive model, bending tests are conducted by utilizing two types of plant roots, which are soybean and barley roots. The results are described in the next subsection, where the material mostly behaves as elastic bodies. Consequently, this subsection utilizes a perfectly elastic model by enforcing a constraint condition,

$$C^{p}_{IJ} = \delta_{IJ} \tag{71}$$

where, δ_{IJ} is the identity matrix, which indicates that no plastic strain is computed during simulations. It is worth noting that this assumption sustains only when the loading stress is smaller than the failure stress of the root tissues.

This section utilizes the Neo-Hookean elastic potential function for root material, which has been utilized for living bio-material such as cell-wall (Huang et al., 2012). As mentioned in the previous subsection, the finite strain theory necessitates an elastic potential function to provide constitutive relationships for a material. The elastic potential function should be chosen so that the stress-strain relationship of material is accurately reproduced. This thesis utilizes the Neo-Hookean elastic potential function since it has been employed to express stress-strain relationships of plant bodies (Huang et al., 2012). The elastic potential function is visible in Eqs. (73) and (74).

$$W = W_1 + W_2 \tag{72}$$

with

$$W_1 = \frac{\Lambda}{4}\left(\epsilon_{\bar{I}\bar{J}\bar{K}}\bar{C}^e_{\bar{1}\bar{I}}\bar{C}^e_{\bar{2}\bar{J}}\bar{C}^e_{\bar{3}\bar{K}} - 1 - 2\ln\sqrt{\epsilon_{\bar{I}\bar{J}\bar{K}}\bar{C}^e_{\bar{1}\bar{I}}\bar{C}^e_{\bar{2}\bar{J}}\bar{C}^e_{\bar{3}\bar{K}}}\right) \tag{73}$$

$$W_2 = \frac{\mu}{2}\left(\bar{C}^e_{\bar{K}\bar{K}} - 3 - 2\ln\sqrt{\epsilon_{\bar{I}\bar{J}\bar{K}}\bar{C}^e_{\bar{1}\bar{I}}\bar{C}^e_{\bar{2}\bar{J}}\bar{C}^e_{\bar{3}\bar{K}}}\right) \tag{74}$$

where Λ and μ are the first and second Lame constants, respectively.

3.2 Constitutive model for soil domain

This subsection discusses the constitutive models of soil domains. There have been developed numerous constitutive models of soils, and some of them have been utilized in terms of the finite strain theory, for instance, the Cam-clay model (Yamakawa et al., 2010). One of the simplest models of soils is a Mohr-Coulomb Drucker-Prager model, which utilizes the Mohr-Coulomb model as a yield function and Drucker-Prager model as a potential plastic function. Both models are visible in Eqs. (55) and (54), respectively. Both models also necessitate an elastic model, and hereby, the Neo-Hookean model is utilized since the model is one of the possible simplest and the widely-used model for elastic behavior ob elasto-plastic models (Hashiguchi and Yamakawa, 2013). Here is the Jacobian matrix of the plastic potential function in terms of return-mapping algorithm.

$$J_{\mu\nu} = \alpha\left[\frac{1}{2}\left(M_{\mu\nu} - \frac{I_1^{\bar{M}}}{3}G_{\mu\nu}\right) + \frac{B_I - 1}{\sqrt{3}B_I + 2\sqrt{3}}G_{\mu\nu}\right] \tag{75}$$

where α is

$$\alpha = 4\Delta\lambda\left[M_{KL} : M_{KL} - \frac{\left(I_1^{\bar{M}}\right)^2}{3} + 3\left(\frac{B_I - 1}{\sqrt{3}B_I + 2\sqrt{3}}\right)^2\right] \tag{76}$$

3.3 Material test for root domain

The root matrix necessitates two elastic moduli; the first and the second Lame constant, which are measured by using a simple bending test. Fig. 4 illustrates a schematic of the bending test where a root is sampled from a straight-root of a soybean seedling, and set on a bending machine. Thereby the relationship between forces P and displacements u are obtained. From the relationship, Young's modulus is estimated. Further, the Poisson's ratio of 0.3 is utilized according to the previous study (Kim et al., 2008).

3.4 Material test for soil domain

This subsection discusses the material tests of soils to determine the parameters of elastic and plastic potential functions. There are two elastic parameters of soil in terms of the MC-DP model; Young's modulus and Poisson's ratio. Young's modulus is measured by using unconfined compression (UC) tests (JGS-0511-2009), which has been used for measuring the Young's modulus-like E_{50} value. This test is conducted for cylinder-shaped specimens of soils, and the stiffness and yield stress under unconfined condition is measured.

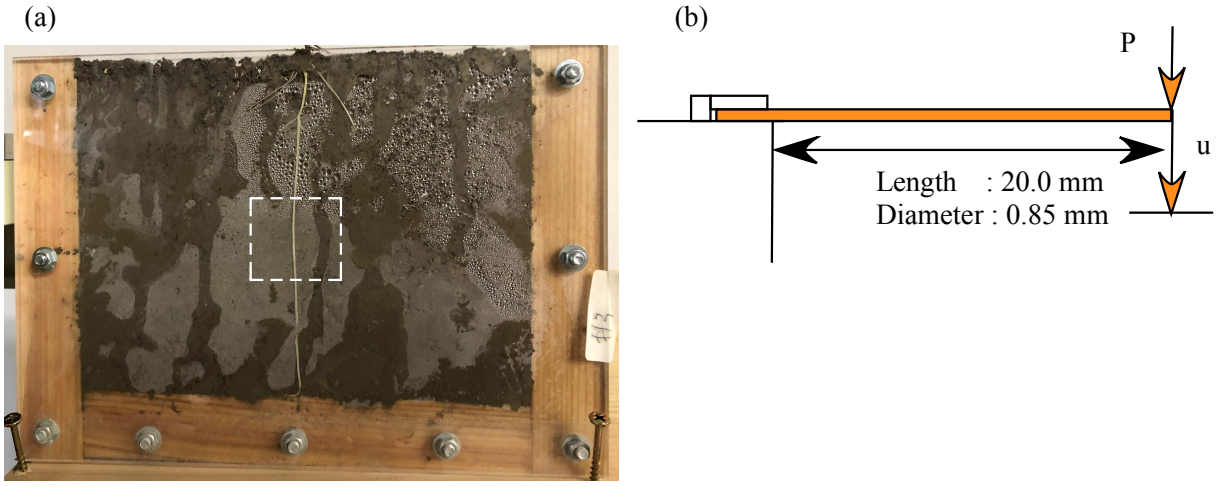

Figure 4: The bending test of a soybean root.

Since plant roots exist in the shallow, unconfined condition, the unconfined compression tests can realize similar stress conditions as the realistic conditions. Besides, the Poisson's ratio is measured by using a simple compression apparatus depicted in Fig. 5, which is similar to the conventional consolidation tests of clays. The presented apparatus loads the vertical pressure on the top of the soil specimen and measures horizontal soil pressure on the side of the specimen. From these results, the soil pressure coefficient is measured, as shown in the left graph of Fig. 5; the Poisson's ratio can be computed from the angle of the regression line.

By contrast, there are three plastic parameters of the MC-DP model, the cohesion c, the frictional angle ϕ, and the dilatancy angle ψ. These parameters are usually measured by using the Direct Shear (DS) tests (JGS-0560-2009 and JGS-0561-2009) or Triaxial Compression (TC) tests (JGS-0521-2009, JGS-0522-2009, JGS-0523-2009, and JGS-0524-2009). The frictional angle ϕ is used for determining the MC model as a yield criterion, and the dilatancy angle ψ is utilized for plastic flow rule to compute the dilatancy effect; noting that the cohesion is utilized for both of yield function and plastic potential function. The material tests and the results are displayed in Chapters 4 and 5.

4 Material test and model of root-soil contact interface

This subsection briefly discusses the numerical model of root-soil interaction for the FE-analysis, which contains novel ideas and approaches, and the detail is presented in Chapters 4 and 6. As can be seen in Fig. 1, it is necessary to model the mechanical interaction of the root and soil domains to precisely predict the deformation of the root-soil system. There are two types of contact phenomena observed in generic contact interfaces: normal and tangential contact. The normal contact indicates the collision at the contact interface, the direction of which is identical to the outer normal vector of the contact interfaces. By contrast, the tangential contact is so-called shear, the direction of which is the same as the tangential vectors of the contact interfaces. It is worth noting that it is possible to define a set of the normal/tangential vectors if and only if the two domains are in contact. Otherwise, sets of normal/tangential vectors of possible contact surfaces are not identical. These two normal vectors are to be preliminarily identified before computing the above contact variables, which is essential for the existence and uniqueness of the solution.

By using the NTS approach, the normal contact and elastic stick of the tangential contact are automatically

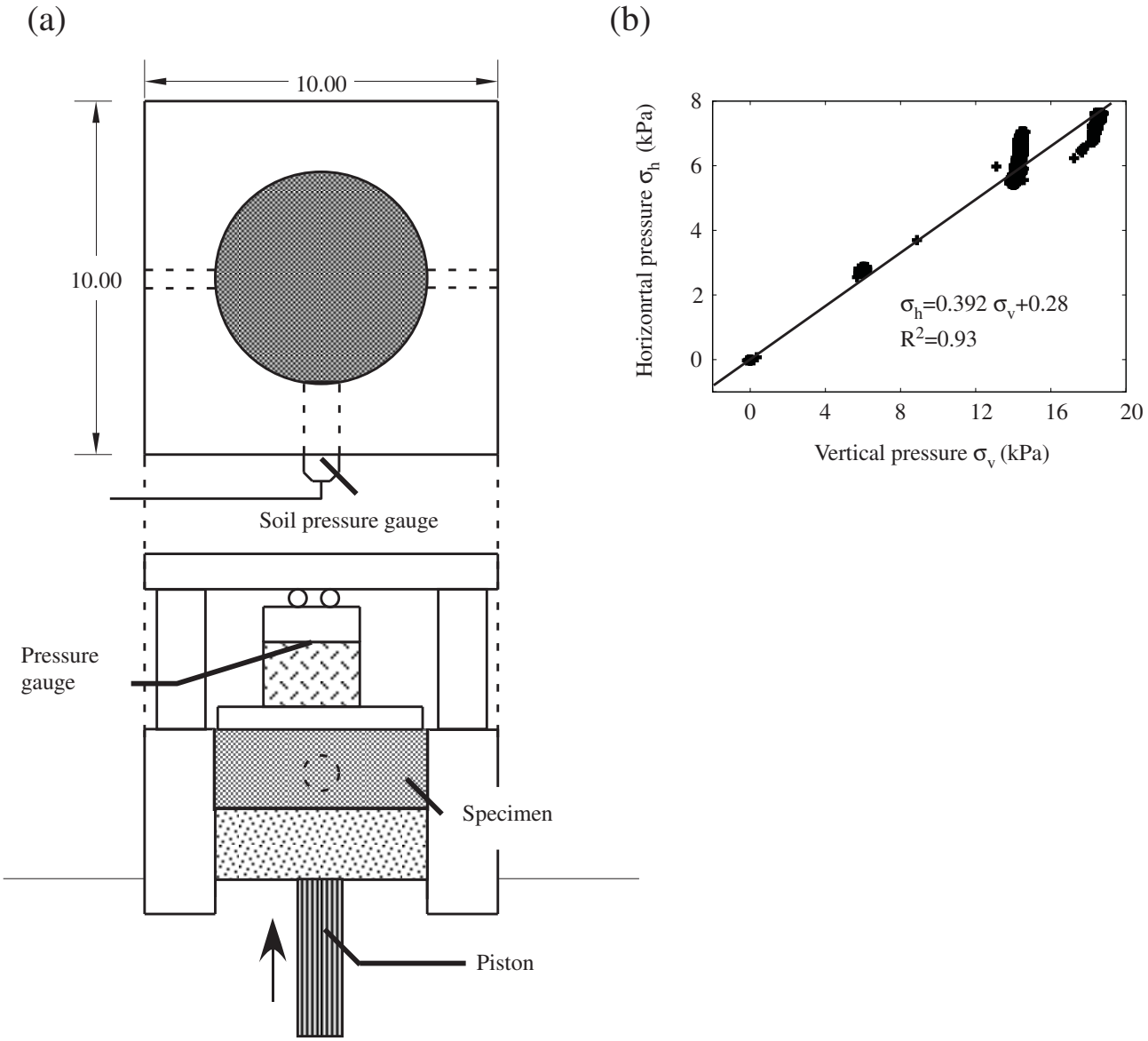

Figure 5: The Poisson's ratio test.

introduced. However, it should be given that the model and parameters of the slip rule of the tangential contact. The detail of the experiment is presented in Chapters 3, 4, and 5.

5 Conclusion

This abstract provides a continuum model for root-soil contact problems based on the finite strain theory and the CCM. The governing equations are derived from the momentum balance, elastic constitutive laws, and plastic flow rules in terms of the finite strain theory, which are essential for root-soil contact problems since both bodies undergo largely deformed processes and often rotate. The CCM is introduced to express root-soil contact interfaces, and the NTS approach is chosen since it is the possible simplest way to express contact, separation, friction, cohesion, and slip in the root-soil interfaces. The NTS approach is also capable of expressing complex root/soil morphologies, which is vital for the application to the practical problems such as numerical simulation of surface erosions in vegetated slopes and lodging of cereals. The concrete expression and material parameters of the root, soil, and root-soil interfaces are visible in the following chapters.

References

Abe, K., and Ziemer, R.R. 1991. Effect of tree roots on a shear zone: modeling reinforced shear stress. Canadian Journal of Forest Research, 21(7): 1012−1019.

Ali, F.H., and Osman, N. 2008. Shear strength of a soil containing vegetation roots. Soils and Foundations, 48(4): 587−596.

Baker, C.J., Berry, P.M., Spink, J.H., Sylvester-Bradley, R., Griffin, J.M., Scott, R.K., and Clare, R.W. 1998. A method for the assessment of the risk of wheat lodging. Journal of Theoretical Biology, 194(4): 587−603.

Baker, C.J., Sterling, M., and Berry, P. 2014. A generalised model of crop lodging. Journal of Theoretical Biology, 363: 1−12.

Berry, P.M., Sterling, M., Spink, J.H., Baker, C.J., Mooney, S.J., Tams, A.R., Ennos, A.R., Rosemaund, A., Wynne, P., and Hr, H. 2004. Understanding and reducing lodging in cereals. Advances in Agronomy, 84(4): 217−271.

Berry, P.M., Spink, J., Sterling, M., and Pickett, A.A. 2003. Methods for rapidly measuring the lodging resistance of wheat cultivars. Journal of Agronomy and Crop Science, 189(6): 390−401.

Bischetti, G.B., Chiaradia, E.A., DAgostino, V., and Simonato, T. 2010. Quantifying the effect of brush layering on slope stability. Ecological Engineering, 36(3): 258−264.

Bizet, F., Bengough, A.G., Hummel, I., Sciences, E., and Dd, D. 2018. 3D deformation field in growing plant roots reveals both mechanical and biological responses to axial mechanical forces. 67(19): 5605−5614.

Das, G.K., Hazra, B., Garg, A., and Ng, C.W.W. 2018. Catena Stochastic hydro-mechanical stability of vegetated slopes : An integrated copula based framework. 160(March 2017): 124−133.

Docker, B.B., and Hubble, T.C.T. 2008. Quantifying root-reinforcement of river bank soils by four Australian tree species. Geomorphology, 100: 401−418.

Dupuy, L.X., Mimault, M., Patko, D., Ladmiral, V., Ameduri, B., Macdonald, M.P., and Ptashnyk, M. 2018. ScienceDirect Micromechanics of root development in soil. Current Opinion in Genetics & Development, 51: 18−25. Elsevier Ltd.

Dupuy, L.X., Fourcaud, T., Lac, P., and Stokes, A. 2007. A generic 3D finite element model of tree anchorage integrating soil mechanics and real root system architecture. American Journal of Botany, 94(9): 1506−1514.

Eab, K.H., Likitlersuang, S., and Takahashi, A. 2015. Laboratory and modelling investigation of root-reinforced system for slope stabilisation. Soils and Foundations, 55(5): 1270−1281. Elsevier.

Endo, T. 1980. Effect of tree roots upon the shear strength of soil. Forest and Forestry Products Research Institute, 14(2): 112−115.

Gray, D.H., and Ohashi, H. 1983. Mechanics of fiber reinforcement in sand. Journal of Geotechnical Engineering, 109(3): 335−353.

Hejazi, S.M., Sheikhzadeh, M., Abtahi, S.M., and Zadhoush, A. 2012. A simple review of soil reinforcement by using natural and synthetic fibers. Elsevier Ltd.

Hughes, T.J.R., Taylor, R.L., Sackman, J.L., Curnier, A., and Kanoknukulchai, W. 1976. A finite element method for a class of contact-impact problems. Computer Methods in Applied Mechanics and Engineering, 8: 249−276.

Liang, T., Bengough, A.G., Knappett, J.A., MuirWood, D., Loades, K.W., Hallett, P.D., Boldrin, D., Leung, A.K., and Meijer, G.J. 2017. Scaling of the reinforcement of soil slopes by living plants in a geotechnical centrifuge. Ecological Engineering,.

Liu, H.W., Feng, S., and Ng, C.W.W. 2016. Computers and Geotechnics Analytical analysis of hydraulic effect of vegetation on shallow slope stability with different root architectures. 80: 115−120.

Liu, W.N., Meschke, G., and Mang, H.A. 2003. Algorithmic stabilization of FE analyses of 2D frictional contact problems with large slip. Computer Methods in Applied Mechanics and Engineering, 192(16−18): 2099−2124.

Mickovski, S.B., Stokes, A., Beek, R. Van, Ghestem, M., and Fourcaud, T. 2011. Simulation of direct shear tests on rooted and non-rooted soil using finite element analysis. Ecological Engineering, 37(10): 1523−1532. Elsevier B.V.

Ookawa, T., Hobo, T., Yano, M., Murata, K., Ando, T., Miura, H., Asano, K., Ochiai, Y., Ikeda, M., Nishitani, R., Ebitani, T., Ozaki, H., Angeles, E.R., Hirasawa, T., and Matsuoka, M. 2010. New approach for rice improvement using a pleiotropic QTL gene for lodging resistance and yield. Nature Communications, 1(8). Nature Publishing Group. doi:10.1038/ncomms1132.

Peric, D., and Owen, D.R.. 1992. Computational model for 3-D contact problems with friction based on the penalty method. International Journal for Numerical Methods in Engineering, 35: 1289−1309.

Rahardjo, H., Harnas, F.R., Indrawan, I.G.B., Leong, E.C., Tan, P.Y., Fong, Y.K., and Ow, L.F. 2014. Understanding the stability of Samanea saman trees through tree pulling, analytical calculations and numerical models. Urban Forestry and Urban Greening, 13(2): 355−364.

Rahardjo, H., Harnas, F.R., Leong, E.C., Tan, P.Y., Fong, Y.K., and Sim, E.K. 2009. Tree stability in an improved soil to withstand wind loading. Urban Forestry and Urban Greening, 8(4): 237−247. Elsevier.

Simo, J.C., and Taylor, R.L. 1986. A returning mapping algorithm for plane stress elastoplasticity. International Journal for Numerical Methods in Engineering, 22(July 1985): 649−670.

Uesugi, M, and Kishida, H. 1986. Influential factors of friction between steel and dry sands. Soils and Foundations, 26(2): 3346.

Vilar, O.M. 2006. A simplified procedure to estimate the shear strength envelope of unsaturated soils. Canadian Geotechnical Journal, 43(10): 1088−1095.

Wriggers, P., Krstulovic-Opara, L., and Korelc, J. 2001. Smooth C1-interpolations for two-dimensional frictional contact problems. International Journal for Numerical Methods in Engineering, 51(12): 1469−1495.

Wriggers, P. 2006. Computational contact mechanics. In Springer, 2nd edition. Springer Berlin Heidelberg, Berlin, Heidelberg.

Zavarise, G., and De Lorenzis, L. 2009. The node-to-segment algorithm for 2D frictionless contact: Classical formulation and special cases. Computer Methods in Applied Mechanics and Engineering, 198(41−44): 3428−3451. Elsevier B.V.

Zavarise, G., and Laura, D.L. 2009. A modified node-to-segment algorithm passing the contact patch test. International Journal for Numerical Methods in Engineering, 79: 379−416.

Zhu, H., Zhang, L.M., Xiao, T., and Li, X.Y. 2017. Computers and Geotechnics Enhancement of slope stability by vegetation considering uncertainties in root distribution. 85: 84−89.